

1. Introduction

2. 计算细节

2.1 DFT 计算细节

Electronic structure calculations were performed with the framework of density functional theory (DFT), as implemented by Vienna ab initio simulation package (VASP)^[1]. The exchange correlation energies were calculated using the Perdew-Burke-Ernzerhof (PBE)^[2] functional within the framework of generalized gradient approximation (GGA)^[3]. The projector augmented wave (PAW)^[4] approach was implemented for core-valence treatment. The simulated structures consisted of four layers of the metal surface, with the bottom two layers of metal atoms and additional ions fixed to preserve the intrinsic properties of the metal, while the top two layers of atoms were allowed to relax to capture the transition from the bulk to the surface properties. A vacuum layer of 10 Å was included to minimize the effects of periodicity. The convergence criteria for electronic self-consistent iteration were set to 1.0×10^{-5} eV, and the ionic relaxation loop was limited for all forces smaller than 0.02 eV/Å for free atoms. For the optimization of the unit cell structure, a cutoff energy of 600 eV and a k-point mesh of $(6 \times 6 \times 6)$ were used, while for the surface structure optimization, a cutoff energy of 400 eV and a k-point mesh of $(3 \times 3 \times 1)$ were employed. The implicit solvent model VASPsol^[5], implemented in VASP, was utilized to capture the influence of electrostatic and dispersion forces on the interaction between solute and solvent. In this model, the relative permittivity of water was set to 78.4.

Adsorption energy is a specific manifestation of electrostatic interactions, which is calculated as:

$$E_{ads} = E(*M) - E(*) - E(M) \quad (1)$$

Where E_{ads} is the adsorption energy and $E(M)$, $E(*)$, and $E(*M)$ represent the

electronic energy of free adsorbate, metal substrate, and adsorbed M on metal surface. Thus, more negative values of binding energies mean stronger adsorption interactions. Gibbs free energies were calculated from DFT total energy corrected by zero-point energy (ZPE), heat capacity (Cp), and entropy (TS), according to the following expression.

$$G = E_{DFT} + E_{ZPE} + \int Cp dT - TS \quad (2)$$

The standard ideal gas method was employed to compute EZPE, $\int Cp dT$ and TS from temperature (298.15K) and pressure (1 atm), and vibrational energies by using the VASPKIT code^[6].

The calculation of the reaction barrier for electrochemical proton-electron transfer reactions is based on the displaced harmonic oscillator model of classical Marcus theory, as established in our previous work^[7]. This calculation involves the free energy change of the reaction (ΔG) and the reorganization energy (λ). In this model, it is assumed that the reorganization energies of the reactants and products are equal.

$$E_a = \frac{\lambda}{4} \left(1 + \frac{\Delta G}{\lambda} \right)^2 \quad (3)$$

The calculation of reaction rates is based on the Marcus-Hush-Chidsey (MHC) theory^[8]:

$$k = \frac{k_B T}{h} \int_{-\infty}^{+\infty} \sqrt{\frac{1}{4\pi\lambda k_B T}} \exp \left(-\frac{(\Delta G + e(\eta - 0.0592 \text{pH}) - \varepsilon + \lambda)^2}{4\lambda k_B T} \right) \frac{1}{1 + \exp \left(\frac{\varepsilon}{k_B T} \right)} d\varepsilon \quad (4)$$

对于反应速率的求解，我们采用稳态近似法，使用 python 中 scipy 库进行求解^[9]。更多动力学计算的详细信息可以在[支持信息](#)中找到。

2.2 Machine learning accelerates the DFT calculation workflow

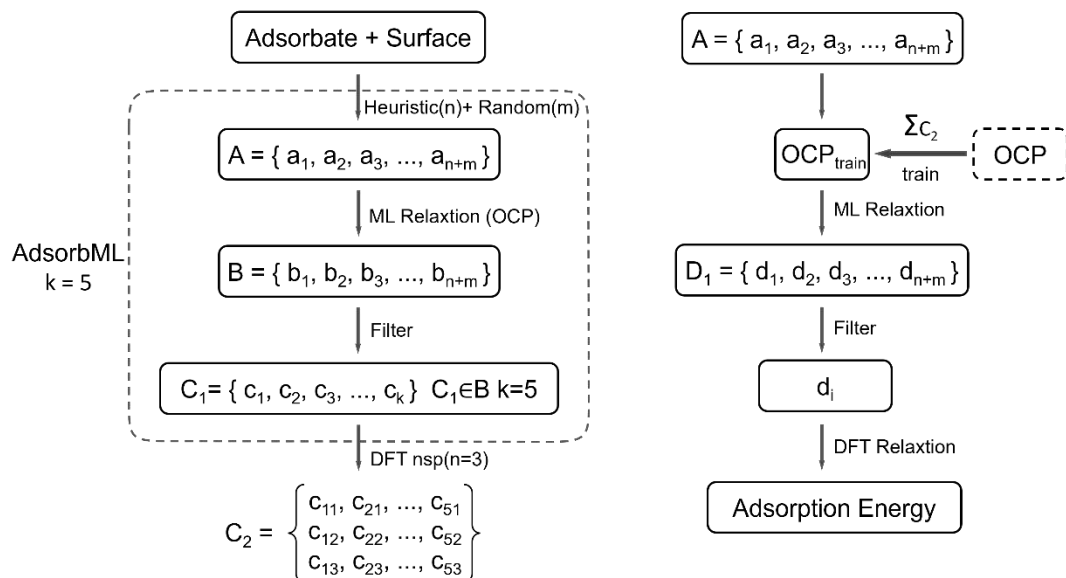


Figure 1. Workflow for Accelerating DFT Calculations Using Machine Learning.

Figure 2.1 illustrates our workflow, which incorporates a fine-tuning step into the AdsorbML framework. This modified workflow will hereafter be referred to as AdsorbML-FT. A molecule adsorbed on a catalyst surface can adopt multiple configurations. Initially, a set of configurations, denoted as Set A, is generated using Pymatgen. This set includes configurations created heuristically (n) as well as those generated randomly (m). Subsequently, the Open Catalyst Project (OCP) framework's machine learning (ML) model is utilized to perform structural relaxation on the configurations in Set A, resulting in an optimized set of configurations, referred to as Set B. From Set B, the five configurations with the lowest ML-predicted energies are selected to form a subset, C1. Each configuration in C1 is then subjected to three single-point density functional theory (DFT) calculations to produce a dataset, C2, consisting of atomic forces and system energies, totaling 15 data points. This process is illustrated on the left side of Figure 2.1.

For a specific adsorbate, this process is repeated on 16 different Cu-based alloy surfaces, and the resulting data ($16 \times C2$) is used to train an ML model specialized for that adsorbate. Using this fine-tuned model, the initial set of configurations A is re-evaluated through ML calculations, yielding a new set of configurations, denoted as D. Finally, the configuration d_i with the lowest energy is selected from D and

subjected to a full DFT structural relaxation calculation to obtain the final adsorption energy. This part of the workflow is shown on the right side of Figure 2.1.

3. Results and Discussion

3.1 Machine learning accelerates the DFT calculation

To accurately and efficiently predict and optimize molecular adsorption configurations on catalyst surfaces, we employed the AdsorbML-FT, which aims to maintain precision while improving computational efficiency. This method accelerates the adsorption configuration optimization process through two primary aspects: firstly, by expediting the relaxation process, and secondly, by more rapidly identifying the global energy minimum. This will be demonstrated using CO adsorption on the Cu₃Al(111) surface as a case study.

1) Accelerated adsorption configuration relaxation

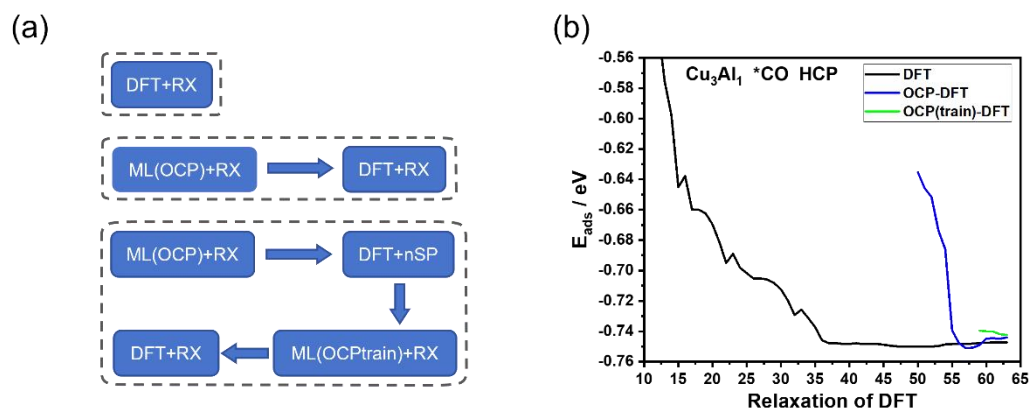


Figure 2. (a) Optimized adsorption structure on the Cu₃Al(111) surface using three different methods. (b) Relaxation process of CO adsorption at the HCP site on the Cu₃Al(111), with the x-axis representing the relaxation steps and the y-axis showing the adsorption energy. The black, blue, and green curves in (b) correspond to the three methods shown from top to bottom in (a).

图2 (a)从上到下分别展示了三种不同的方法来优化计算 Cu_3Al_1 上 CO 吸附结构的能量。方案一为直接使用 DFT 弛豫计算，结果为(a)中的黑线。方案二为使用 ML 弛豫后再用 DFT 进行弛豫计算，结果为(b)中的蓝线。方案三为使用微调后的 ML 加 DFT 弛豫计算，结果为(b)中的绿线。从能量收敛曲线可以看出，AdsorbML-FT 方法（绿色曲线）展现出最快的收敛速度，表明经过微调后的模型能够显著加速吸附构型的弛豫过程，有效减少达到能量收敛所需的计算步数。

2) 加速催化剂表面全局最优的寻找

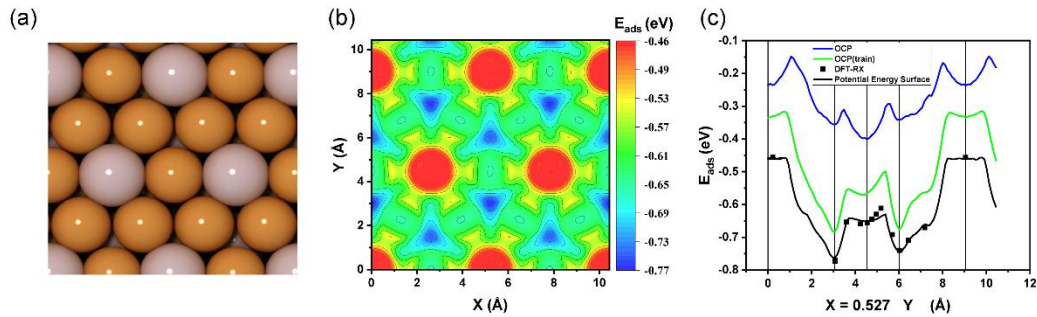


Figure 3. (a) Top view of the $\text{Cu}_3\text{Al}_1(111)$ surface. (b) Adsorption potential energy surface of CO on the surface shown in (a). (c) Adsorption energy profile along the $x = 0.527$ line in (b), predicted by three different models.

The determination of the global energy minimum is crucial for understanding catalytic reaction mechanisms and designing highly efficient catalysts. Using the catalytic surface depicted in Figure 3 as an example, we investigated the application of AdsorbML-FT in searching for the global minimum energy configuration. Initially, the catalyst surface in Figure 3a was divided into a 100×100 grid, with the z -coordinate fixed. Data from relaxation using a conventional heuristic method were used to train the model, which was then employed to relax and locate the minimum energy point in the z -direction, generating the **adsorption potential energy surface (PES)** shown in Figure 3b. The accuracy of this PES was used as a benchmark to compare the performance of two approaches in predicting the global energy minimum.

As illustrated in Figure 3c, the black curve represents the adsorption potential energy profile along the line $x = 0.527$ in Figure 3b, with black discrete points

indicating DFT validation results, confirming the accuracy of the PES. The blue curve in Figure 3c depicts the potential energy profile predicted by the original ML model (OCP), while the green curve represents the profile predicted by the fine-tuned model (OCP(train)). The results demonstrate that the potential energy profile predicted by the fine-tuned model (green curve) exhibits closer agreement with the benchmark curve (black), indicating that the fine-tuned model can more accurately identify the global energy minimum.

For a systematic assessment of the computational efficiency enhancement offered by the AdsorbML-FT method, we compared its performance with a traditional heuristic approach in optimizing the adsorption configurations of CO, CHO, and COH molecules on a set of 16 different alloy surfaces (Cu₃M1(111), M representing various alloy elements). A heuristic approach was used to generate initial adsorption structures using Pymatgen, which were subsequently relaxed using DFT calculations.

Table 1. Conventional Heuristic vs. AdsorbML-FT

Method	Force (eV/Å)	N _{sp}	N _{RX}	Total
Heuristic	0.02	0	32,680	32,680
AdsorbML-FT	0.02	537	805	1,342
AdsorbML-FT	0.05	537	332	869

When a force convergence criterion of 0.02 eV/Å is employed, the traditional heuristic approach necessitates 32,680 DFT single-point calculations, as indicated in Table 1. In contrast, the AdsorbML-FT method necessitates only 537 single-point energy calculations and 805 structural relaxations, totaling 1,342 steps, thereby achieving a 24.4-fold improvement in computational efficiency. The root mean square error (RMSE) between the two methods is 0.01 eV. The theoretical number of single-point calculations is given by $3 * 16 * C_2$, where this factor accounts for instances where distinct initial adsorption configurations converge to the same final relaxed structure.

Relaxing the force convergence criterion to 0.05 eV/Å reduces the required structural relaxation steps for the AdsorbML-FT method to 332, resulting in a total of 869 computational steps. Although this looser convergence criterion introduces a slight increase in the RMSE of the adsorption energy calculation to 0.014 eV compared to the 0.02 eV/Å criterion, the computational efficiency is significantly enhanced, achieving a 58.4-fold speedup relative to traditional methods. Our results demonstrate that by judiciously adjusting computational parameters, the AdsorbML-FT method can substantially improve computational efficiency while maintaining acceptable accuracy. Detailed information regarding model training can be found in the Supporting Information.

3.2 CORR on Cu(111)

The electrocatalytic CORR involves multiple intermediates and reaction steps, making its mechanism particularly complex. A thorough understanding of reaction pathways and rate-determining steps is crucial for designing efficient catalysts. As an important kinetic analysis method, the steady-state approximation method can effectively handle complex reaction systems. This work combines machine learning accelerated computations and Marcus transition state theory to efficiently acquire kinetic parameters for CORR on copper-based catalysts. Cu, as a CORR catalyst, has unique catalytic ability. The following is a detailed study of CORR on Cu.

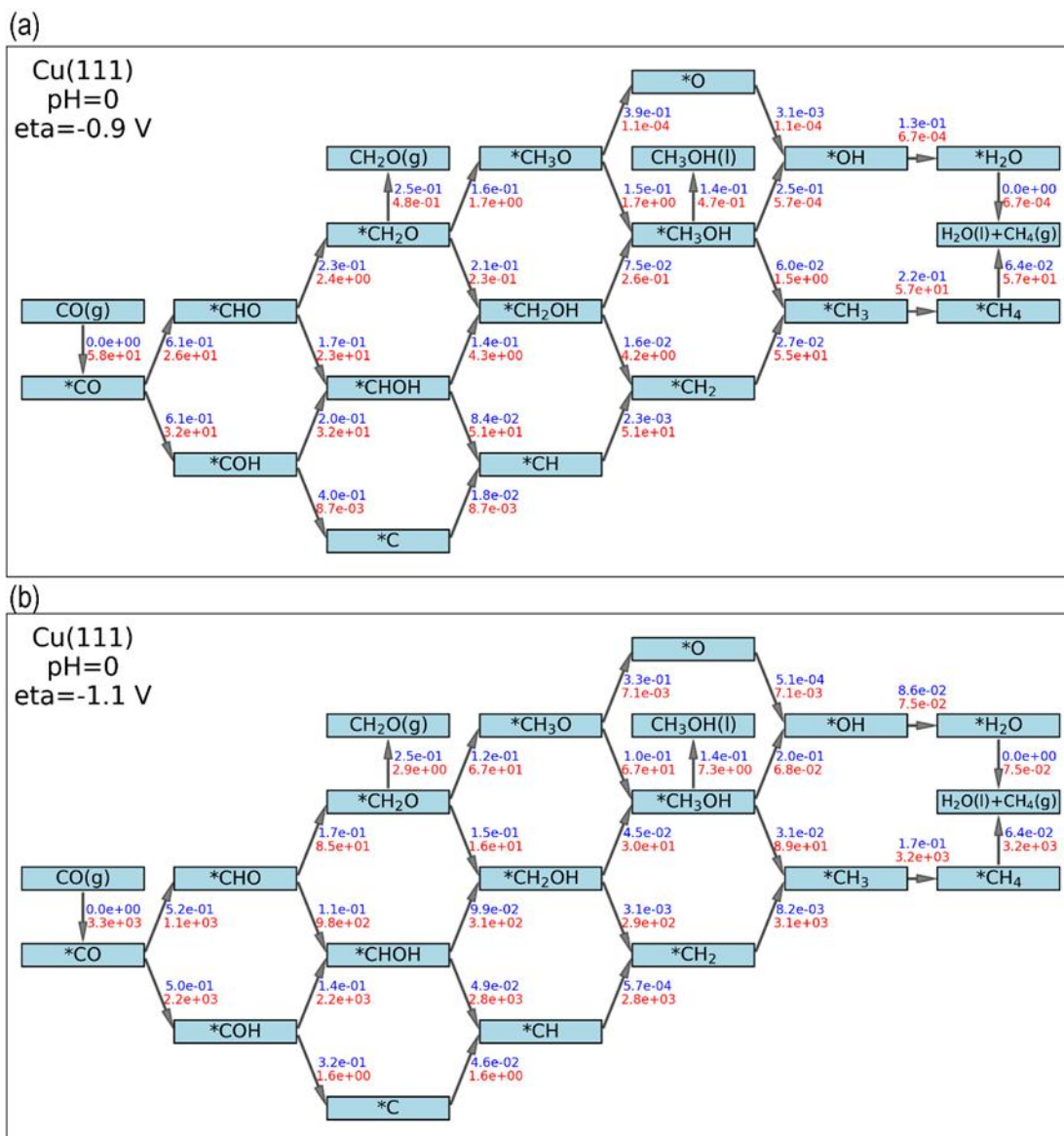
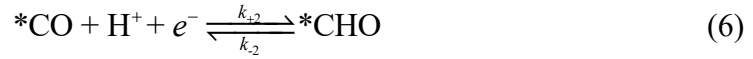
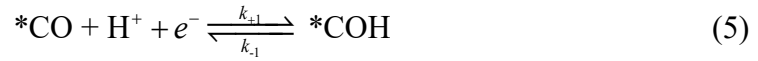


Figure 4. Steady-state kinetic analysis of CO reduction on Cu(111) at (a) -0.9 V and (b) -1.1 V vs. RHE. Blue: activation barriers (eV); Red: reaction rates. Boundary conditions: CO(g), H₂O(l) = 1; CH₂O(g), CH₃OH(l), CH₄(g), pH = 0.

The formation of CHO and COH from CO is a crucial step in the CORR. As depicted in blue in Figure 4a, calculations based on Marcus transition state theory reveal that the activation barriers for the formation of CHO (0.614 eV) and COH (0.611 eV) are very similar at a potential of -0.9 V. This finding is in excellent agreement with the results reported by Zhao et al.^[11], who demonstrated that the CHO

and COH pathways contribute equally to the CORR at a potential of -0.9 V. As shown in red in Figure 4a, the reaction rates of the CHO pathway and the COH pathway, calculated using the steady-state approximation method, are very close to each other. The main reason for this is that the overall reaction rate of CORR can be determined by the formation of CHO and COH from CO, as expressed in the following equation:



$$r_{CO} = k_{+1} * \theta_{CO} [H^+] - k_{-1} * \theta_{COH} + k_{+2} * \theta_{CO} [H^+] - k_{-2} * \theta_{CHO} \quad (7)$$

Where θ represents the surface coverage and $[H^+]$ represents the hydrogen ion concentration in solution, which is assumed to be 1 here. When the potential is -0.9 V, the ΔG for equations (5) and (6) is less than 0, indicating that the forward reaction rate (k_+) is greater than the reverse reaction rate (k_-). Furthermore, the CO coverage approaches 1 according to the steady-state approximation. The overall reaction rate is the sum of k_+ for equations (5) and (6), where k_+ is determined by the activation energy of the forward reaction. This explains why the first step of CO reaction is widely reported as a method for evaluating catalyst activity in the vast majority of studies.

Additionally, the product selectivity of CORR on the Cu(111) surface was investigated. As illustrated in Figure 4b, computational results indicate that at a potential of -0.9 V, the ratio of formation rates between methane and methanol ($r(CH_4)/r(CH_3OH)$) is 121, differing by approximately two orders of magnitude. It is important to note that due to the zero-concentration boundary condition for products in the model, the calculated results can be sensitive to the actual product concentrations in the solution, particularly when formation rates are low. When assuming a methanol concentration of 10^{-3} in the solution, $r(CH_3OH)$ decreases to 0.03, expanding the difference in $r(CH_4)/r(CH_3OH)$ to three orders of magnitude. As the methanol concentration in the solution further increases, $r(CH_3OH)$ continues to decrease, ultimately resulting in methane as the predominant product. Previous experimental studies have reported varying results regarding CO reduction on Cu(111)

surfaces. Hori et al. demonstrated that CO reduction on Cu(111) primarily yields methane [12]. In contrast, Kendra et al. observed the simultaneous production of methane and methanol on copper electrodes, with $r(\text{CH}_3\text{OH})$ approximately four orders of magnitude lower than $r(\text{CH}_4)$ [13]. The computational results presented in this study offer a potential explanation for these observed discrepancies in the literature. Moreover, at a potential of -1.1 V (as shown in Figure 4b), the calculated $r(\text{CH}_4)/r(\text{CH}_3\text{OH})$ ratio is 3200/7.3. This result closely aligns with the predictions made by Hussain et al. for room temperature conditions (3 orders of magnitude) and experimental findings on Cu(111) surfaces (2.5 orders of magnitude) [14]. These findings suggest that employing the steady-state approximation in the analysis of complex reaction networks can more accurately reflect the true reaction dynamics.

3.3 CORR on $\text{Cu}_3\text{M}_1(111)$

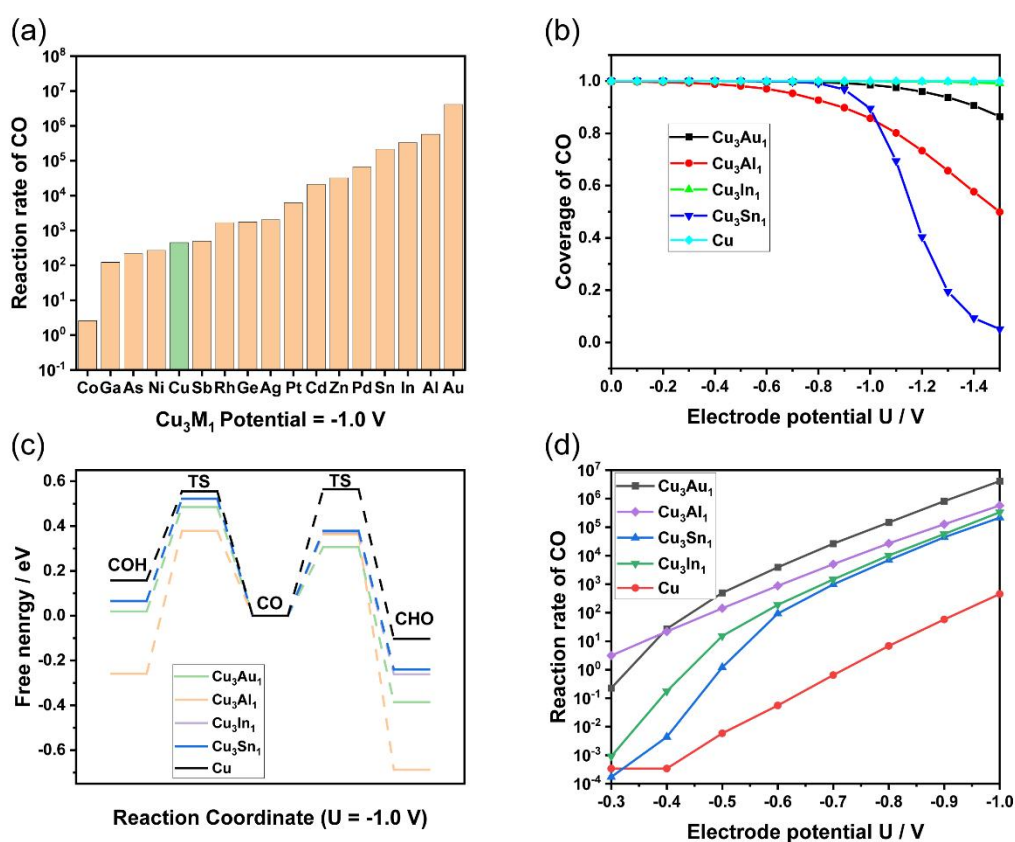


Figure 5. (a) CO reduction rates on Cu_3M_1 catalysts at -1.0 V vs. RHE. The x-axis

represents the alloying element M, with Cu representing pure copper. (b) Potential-dependent CO reduction rates on Cu₃Au₁, Cu₃Al₁, Cu₃In₁, Cu₃Sn₁, and pure Cu catalysts. (c) Potential-dependent CO coverage on these catalysts. (d) Energy diagrams for the formation of CHO and COH intermediates from CO on the five catalysts at -1.0 V vs. RHE, where TS denotes the transition state.

To explore the impact of alloying elements on the CORR, Cu₃M₁ alloy models were constructed by substituting one copper atom in the face-centered cubic (fcc) unit cell of Cu with a different element (M). The alloying elements considered include Co, Ga, As, Ni, Cu, Sb, Rh, Ge, Ag, Pt, Cd, Zn, Pd, Sn, In, Al, and Au (details on formation energies and stability, as determined by convex hull analysis, are provided in the Supporting Information). Using the steady-state approximation method, the CORR activity of these 16 Cu₃M₁ alloys was evaluated at a potential of -1.0 V. As shown in Figure 5a, alloys with Sb, Rh, Ge, Ag, Pt, Cd, Zn, Pd, Sn, In, Al, and Au exhibit enhanced CORR activity compared to pure Cu, with Cu₃Sn₁, Cu₃In₁, Cu₃Al₁, and Cu₃Au₁ showing particularly high activity.

Figure 5(b) illustrates the CO surface coverage as a function of potential for pure Cu and the four most active alloys. At -1.0 V, CO adsorption dominates the catalyst surface, making the conversion of CO to CHO and COH the rate-determining step. The reaction rate is primarily governed by the activation energy for CHO and COH formation.

Figure 5(c) compares the energy profiles for CHO and COH formation on pure Cu and the Cu₃Sn₁, Cu₃In₁, Cu₃Al₁, and Cu₃Au₁ alloys.

These four alloys display lower free energies and activation barriers for both pathways compared to pure Cu, with the CHO pathway having the lower activation energy.

Figure 5d illustrates the relationship between the CO reduction rate and the applied potential. It is evident that under conditions where significant CO reduction occurs, the catalytic performance of Cu₃Sn₁, Cu₃In₁, Cu₃Al₁, and Cu₃Au₁ is

markedly superior to that of pure Cu. The following sections provide a detailed discussion of the effects of applied potential and composition on product selectivity.

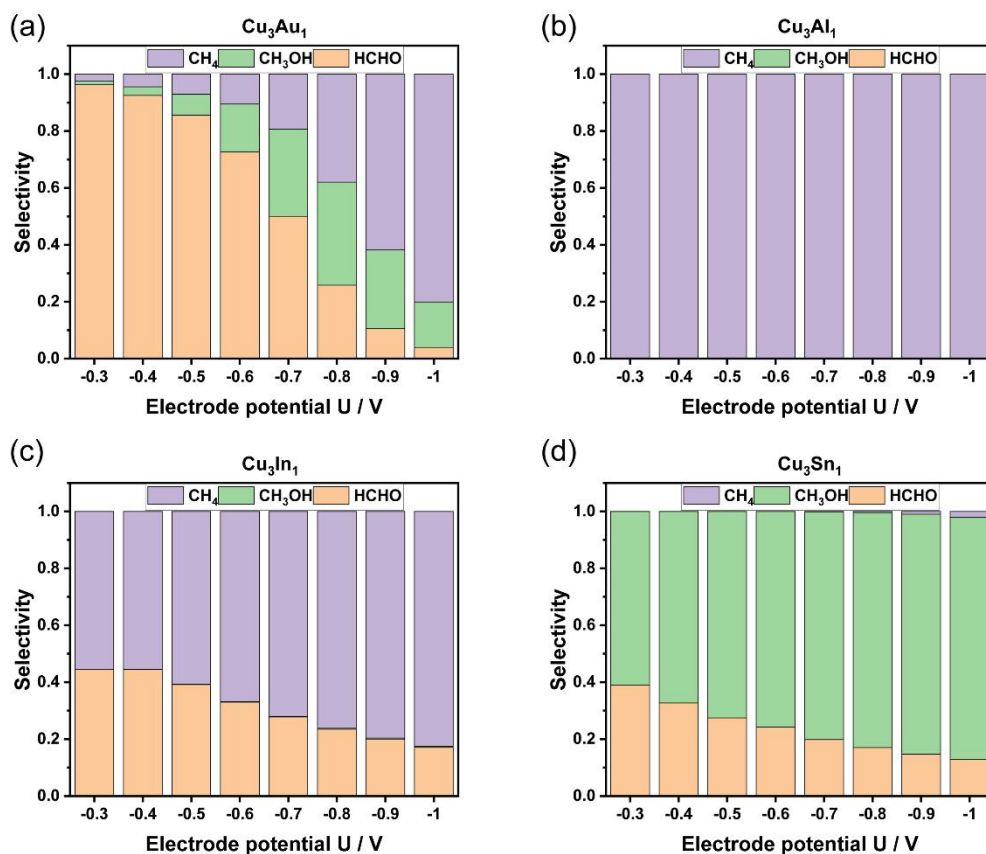


Figure 6 (a)-(d) illustrate the selectivity of C1 products from CO electroreduction on Cu₃Au₁, Cu₃Al₁, Cu₃In₁, and Cu₃Sn₁ alloy catalysts within a potential range of -0.3 V to -1.0 V vs. RHE.

对于合金上 CO 还原反应的 C₁ 产物的选择性, 我们使用法拉第效率 (FE), 公式如下:

$$FE_i = \frac{j_i}{j_{\text{total}}} = \frac{z_i F r_i}{\sum_i z_i F r_i} \quad (6)$$

式中 r_i 为 C₁ 产物 i 的反应速率, n 为 CO 还原反应的电子数。如图 6 所示, Cu₃Au₁ 在较低过电位 (-0.3 至 -0.5 V vs. RHE) 下主要产物为甲醛, 而在较高过电位 (-0.6 至 -1 V vs. RHE) 下则更倾向于生成甲烷, 这表明其产物选择性具有明显的电位依赖性。相比之下, Cu₃Al₁ 在整个测试电位范围内几乎只生成甲烷。Cu₃In₁ 主要

生成甲烷和甲醛，且随着电位负移，甲烷选择性略有增加。而 Cu_3Sn_1 则主要生成甲醇和甲醛。值得注意的是，所有催化剂体系中，甲醛的选择性均随电位的负移而降低，而甲烷的选择性则逐渐升高。这主要与中间产物的脱附和进一步质子电子转移反应有关。在特定的电位范围内，电位越负，相应反应的吉布斯自由能越低，从而更有利于质子-电子转移反应的进行。

为了进一步探究催化剂组成对产物选择性的影响机制，分析了不同催化剂表面对反应中间体（O、H、CO）的吸附强度。根据计算结果（详见 SI），我们发现催化剂表面对氧的吸附强度与 C-O 键的断裂密切相关。较强的氧吸附有利于 C-O 键的断裂，这与 Vasileff 等人的研究结果一致^[15]。类似地，氢在催化剂表面的吸附强度也会影响 C-H 键的形成，从而影响产物选择性（在此仅考虑质子电子转移过程）。对 CO 和 O 具有较强吸附能力的催化剂， CH_2O 和 CH_3OH 的吸附也较强，导致其较难脱附，这进一步提高了甲烷的选择性。对于图 6 中的四种催化剂， Cu_3Al_1 由于其对氧的强吸附，表现出极高的甲烷选择性。 Cu_3In_1 的氧吸附强度虽次于 Cu_3Al_1 ，但仍高于 Cu_3Au_1 和 Cu_3Sn_1 ，因此其甲烷选择性也较高。 Cu_3Au_1 和 Cu_3Sn_1 之间的差异可能源于 Cu_3Au_1 对氢的吸附较弱，导致 C-H 键更容易形成，从而降低了反应的活化能。

在已有的文献报道中， Cu_3Au_1 能够高效地将 CO 转化为甲烷^[16]，而其他一些报道 Cu-Au 合金则表现出对甲醇生成的催化活性^[17]。与之相对的，我们计算的 Cu_3Au_1 上预测了甲醇与甲烷的生成。对于 Cu_3Al_1 合金，文献指出 Cu_3Al 合金催化剂更倾向于促进 C_2 烃类的形成^[18]，尽管我们的研究范围仅限于 C_1 产物，但总体而言，即使仅考虑 C_1 产物，我们的数据依然揭示了 Cu_3Al_1 相较于纯铜展现出更卓越的催化活性。

4. Conclusion

本研究通过结合机器学习与 Marcus 理论，系统地研究了一系列合金在 CORR 中的催化性能。在热力学方面，借助机器学习的加速作用提升 DFT 的计算效率。在动力学方面，采用 Marcus 理论，仅需通过 DFT 计算一个单点能量，就能推导出不同电压下反应的活化能。随后，基于稳态近似法构建了微观动力学模型，并成功验证了 Cu(111) 表面上 CORR 结果与实验数据的高度吻合性。将

该微观动力学模型应用在合金筛选中，最终在 16 种 Cu_3M_1 合金中成功筛选出具有优异 CORR 活性的 Cu_3Au_1 和 Cu_3Al_1 合金，并揭示了 CO、H、O 吸附能对催化剂选择性的影响。不足的是，本研究的局限性在于仅考虑了 C_1 路径的反应机制。未来研究将进一步探索 C_2 路径，以更全面地理解反应机制。总体而言，本工作为理解复合材料在 CO 电催化反应中的结构-性能关系提供了新的见解，并为高效的理论计算提供了一种框架基础。

- [1] a) G. Kresse, J. Furthmüller, *Comput. Mater. Sci.* **1996**, 6, 15-50; b) G. Kresse, D. Joubert, *Phys Rev B* **1999**, 59, 1758-1775.
- [2] J. P. Perdew, K. Burke, M. Ernzerhof, *Phys. Rev. Lett.* **1996**, 77, 3865-3868.
- [3] J. P. Perdew, J. A. Chevary, S. H. Vosko, K. A. Jackson, M. R. Pederson, D. J. Singh, C. Fiolhais, *Phys. Rev. B* **1992**, 46, 6671-6687.
- [4] P. E. Blochl, *Phys. Rev. B* **1994**, 50, 17953-17979.
- [5] a) K. Mathew, R. Sundararaman, K. Letchworth-Weaver, T. A. Arias, R. G. Hennig, *J. Chem. Phys.* **2014**, 140, 084106; b) K. Mathew, V. S. C. Kolluru, S. Mula, S. N. Steinmann, R. G. Hennig, *J. Chem. Phys.* **2019**, 151, 8.
- [6] V. Wang, N. Xu, J. C. Liu, G. Tang, W. T. Geng, *Comput. Phys. Commun.* **2021**, 267, 19.
- [7] a) S.-Q. Xiang, J.-L. Shi, S.-T. Gao, W. Zhang, L.-B. Zhao, *ACS Catal.* **2021**, 11, 2422-2434; b) S. T. Gao, S. Q. Xiang, J. L. Shi, W. Zhang, L. B. Zhao, *Phys. Chem. Chem. Phys.* **2020**, 22, 9607-9615; c) S.-Q. Xiang, S.-T. Gao, J.-L. Shi, W. Zhang, L.-B. Zhao, *J. Catal.* **2021**, 393, 11-19.
- [8] a) R. A. J. T. J. o. c. p. Marcus, *J. Chem. Phys.* **1956**, 24, 966-978; b) N. S. J. T. J. o. C. P. Hush, *J. Chem. Phys.* **1958**, 28, 962-972; c) C. E. J. S. Chidsey, *Science* **1991**, 251, 919-922.
- [9] P. Virtanen, R. Gommers, T. E. Oliphant, M. Haberland, T. Reddy, D. Cournapeau, E. Burovski, P. Peterson, W. Weckesser, J. Bright, S. J. van der Walt, M. Brett, J. Wilson, K. J. Millman, N. Mayorov, A. R. J. Nelson, E. Jones, R. Kern, E. Larson, C. J. Carey, Í. Polat, Y. Feng, E. W. Moore, J. VanderPlas, D. Laxalde, J. Perktold, R. Cimrman, I. Henriksen, E. A. Quintero, C. R. Harris, A. M. Archibald, A. H. Ribeiro, F. Pedregosa, P. van Mulbregt, A. Vijaykumar, A. P. Bardelli, A. Rothberg, A. Hilboll, A. Kloeckner, A. Scopatz, A. Lee, A. Rokem, C. N. Woods, C. Fulton, C. Masson, C. Häggström, C. Fitzgerald, D. A. Nicholson, D. R. Hagen, D. V. Pasechnik, E. Olivetti, E. Martin, E. Wieser, F. Silva, F. Lenders, F. Wilhelm, G. Young, G. A. Price, G.-L. Ingold, G. E. Allen, G. R. Lee, H. Audren, I. Probst, J. P. Dietrich, J. Silterra, J. T. Webber, J. Slavič, J. Nothman, J. Buchner, J. Kulick, J. L. Schönberger, J. V. de Miranda Cardoso, J. Reimer, J. Harrington, J. L. C. Rodríguez, J. Nunez-Iglesias, J. Kuczynski, K. Tritz, M. Thoma, M. Neville, M. Kümmerer, M. Bolingbroke, M. Tartre, M. Pak, N. J. Smith, N. Nowaczyk, N. Shebanov, O. Pavlyk, P. A. Brodtkorb, P. Lee, R. T. McGibbon, R. Feldbauer, S. Lewis, S. Tygier, S. Sievert, S. Vigna, S. Peterson, S. More, T. Pudlik, T. Oshima, T. J. Pingel, T. P. Robitaille, T. Spura, T. R. Jones, T. Cera, T. Leslie, T. Zito, T. Krauss, U. Upadhyay, Y. O. Halchenko, Y. Vázquez-Baeza, C. SciPy, *Nat. Methods* **2020**, 17, 261-272.
- [10] S. P. Ong, W. D. Richards, A. Jain, G. Hautier, M. Kocher, S. Cholia, D. Gunter, V. L. Chevrier, K. A. Persson, G. J. C. M. S. Ceder, *Comput. Mater. Sci.* **2013**, 68, 314-319.
- [11] Q. Zhao, J. M. P. Martirez, E. A. Carter, *J. Am. Chem. Soc.* **2021**, 143, 6152-6164.
- [12] Y. Hori, R. Takahashi, Y. Yoshinami, A. Murata, *J. Phys. Chem. B* **1997**, 101, 7075-7081.
- [13] K. P. Kuhl, T. Hatsukade, E. R. Cave, D. N. Abram, J. Kibsgaard, T. F. Jaramillo, *J. Am. Chem. Soc.* **2014**, 136, 14107-14113.
- [14] J. Hussain, H. Jónsson, E. Skúlason, *ACS Catal.* **2018**, 8, 5240-5249.

- [15] A. Vasileff, C. Xu, Y. Jiao, Y. Zheng, S.-Z. Qiao, *Chem* **2018**, *4*, 1809-1831.
- [16] a) X. Wang, P. Ou, J. Wicks, Y. Xie, Y. Wang, J. Li, J. Tam, D. Ren, J. Y. Howe, Z. Wang, A. Ozden, Y. Z. Finfrock, Y. Xu, Y. Li, A. S. Rasouli, K. Bertens, A. H. Ip, M. Graetzel, D. Sinton, E. H. Sargent, *Nat. Commun.* **2021**, *12*, 3387; b) A. Guan, Q. Wang, Y. Ji, S. Li, C. Yang, L. Qian, L. Zhang, L. Wu, G. Zheng, *J. Mater. Chem. A* **2021**, *9*, 21779-21784.
- [17] a) J. Mosrati, T. Ishida, H. Mac, M. Al - Yusufi, T. Honma, M. Parliniska - Wojtan, Y. Kobayashi, A. Klyushin, T. Murayama, A. M. J. A. C. Abdel - Mageed, *Angew. Chem.* **2023**, *135*, e202311340; b) Y. Xiao, L. Tang, W. Zhang, C. Shen, *Comput. Mater. Sci.* **2021**, *192*, 110402.
- [18] a) M. Zhong, K. Tran, Y. Min, C. Wang, Z. Wang, C.-T. Dinh, P. De Luna, Z. Yu, A. S. Rasouli, P. Brodersen, S. Sun, O. Voznyy, C.-S. Tan, M. Askerka, F. Che, M. Liu, A. Seifitokaldani, Y. Pang, S.-C. Lo, A. Ip, Z. Ulissi, E. H. Sargent, *Nature* **2020**, *581*, 178-183; b) T. T. H. Hoang, S. Verma, S. Ma, T. T. Fister, J. Timoshenko, A. I. Frenkel, P. J. A. Kenis, A. A. Gewirth, *J. Am. Chem. Soc.* **2018**, *140*, 5791-5797.